Monitoring of Maskun landslide and determining its quantitative relationship to different climatic conditions using D-InSAR and PSI techniques

Mohsen Pourkhosravani, Ali Mehrabi, Saied Pirasteh & Reza Derakhshani

Published online: 20 Apr 2022.

Submit your article to this journal

Article views: 184

View related articles

View Crossmark data

Taylor & Francis
Taylor & Francis Group

Monitoring of Maskun landslide and determining its quantitative relationship to different climatic conditions using D-InSAR and PSI techniques

Mohsen Pourkhosravani[a] (iD), Ali Mehrabi[a] (iD), Saied Pirasteh[b] (iD) and Reza Derakhshani[c,d] (iD)

[a]Department of Geography, Shahid Bahonar University of Kerman, Kerman, Iran; [b]Department of Geoinformatics and Surveying, Faculty of Geosciences and Environmental Engineering (FGEE), Southwest Jiaotong University, Chengdu, China; [c]Department of Geology, Shahid Bahonar University of Kerman, Kerman, Iran; [d]Department of Earth Sciences, Utrecht University, Utrecht, The Netherlands

ABSTRACT

Climate change has resulted in severe landslides in Maskun, Iran. This study evaluates and monitors the displacement caused by the landslide mass in Bam using Interferometry Synthetic Aperture Radar (DInSAR) and Persistent Scatterer Interferometry (PSI) techniques, as well as identifies relationships between climatic conditions and mass displacement. Temperature and precipitation data from 2007 to 2019 were combined with satellite images and the DInSAR method was used to determine the mass displacement differences after selecting eighteen radar images from the ASAR sensor of the ENVISAT satellite. Additionally, Sentinel 1 satellite images were acquired and analyzed using the PSI method from November 5, 2014, to June 24, 2019. The highest displacement level at the surface of the Maskun landslide mass was then extracted. The ASAR images show a monthly displacement rate of 7.3 mm. The smallest displacement, on the other hand, occurred between May and September 2009, at a rate of 3.1 mm/month. PSI results also revealed that the maximum Line Of Sight (LOS) velocities detected by PSI are -64.5 mm/yr (away from the satellite) and 32.45 mm/yr (toward the satellite). Rainfall is one of the main triggers for increasing the deformation of the Maskun landslide according to the time-series analysis.

1. Introduction

Landslide is one of the continuous external processes that causes the ground surface to be deformed and creates certain landforms. This phenomenon occurs in areas where the shear stress of materials is greater than the shear strength, which is commonly referred to as instability or slope failure (Ali et al. 2003). Landslides are one of

CONTACT Reza Derakhshani ✉ r.derakhshani@uu.nl

the most destructive natural hazards that threaten human lives and influence the socioeconomic condition of many countries. Landslides pose long-lasting threats to humans and their property and are detrimental to the environment in general (Chang et al. 2018; Azarafza, Azarafza et al. 2021). Because of its specific geologic, morphologic, climatic, and tectonic settings, Iran is one of the most landslide-prone areas in the world. By 2000, approximately 2600 landslides, which were responsible for 162 deaths, 176 fully destroyed houses, and 170 damaged roads, were detected and mapped by experts from various government agencies in the country (Akbarimehr et al. 2013).

For this reason, the identification and the impact of the active Quaternary slope movements, as an erosion phenomenon, is of particular importance in posing threats to the residential areas, farms, reservoirs, dams, and the destruction of access roads. Since the landslide occurrence cannot be easily understood due to slow movements, measuring the movement level requires specific studies and tools. Researchers have used various techniques and tools to identify and monitor landslides (Akbarimehr et al. 2013; Chang et al. 2018; Azarafza et al. 2020; Azarafza et al. 2021). Nowadays, the accessibility of large stacks of SAR data from historical and new generation satellite sensors authorizes spatially and temporally detection of landslide displacements at a local and regional scale with improved punctuality and accuracy (Bianchini et al. 2013). However, the behavior of mass displacement varies because of climatic conditions and geographical locations. A few researchers have studied the relationships between mass displacement and climatic conditions (Zhu et al. 2020).

The radar interferometry technique (D-InSAR), with its extensive, frequent, and continuous land cover as well as high spatial and temporal resolution, has been provided as one of the most accurate (with millimeter-level accuracy) and cost-effective remote sensing techniques for detecting and displaying the displacements that occur on the ground surface (Schlögel et al. 2015; Zhang et al. 2020; Mehrabi et al. 2021). Furthermore, the ability of this technique to detect and monitor the mass movement phenomenon can be found in several studies (Gabriel et al. 1989; Farina et al. 2006; Bovenga et al. 2012; Crosetto et al. 2013; Liu et al. 2013; Mehrabi et al. 2020; Mehrabi et al. 2021; Novellino et al. 2021). For example, they used D-InSAR to locate and monitor landslide mass movements in China's Jinsha River. Furthermore, they generated moving displacement maps for two time periods. Nevertheless, more related studies also can be found (Wang et al. 2013; Bru et al. 2017; Chaabani and Deffontaines 2020; Hou and Zhang 2020; Zhang et al. 2020).

However, the objective of this study is to monitor the displacement level due to the landslide phenomenon in the Maskun-Bam region of Iran using the radar interferometry technique. In addition, this study intends to consider the behavior of slippery masses and overcome the lack of investigation into the relationships between the displacement rate of a landslide and weather conditions quantitatively.

2. Study area and datasets

The study landslide is located in the south of Maskun in the Dehbakri district of Bam, Iran. The coordination of this area is 57° 50′ to 58° E and 28° 55′ to 29° 4′ N. The study
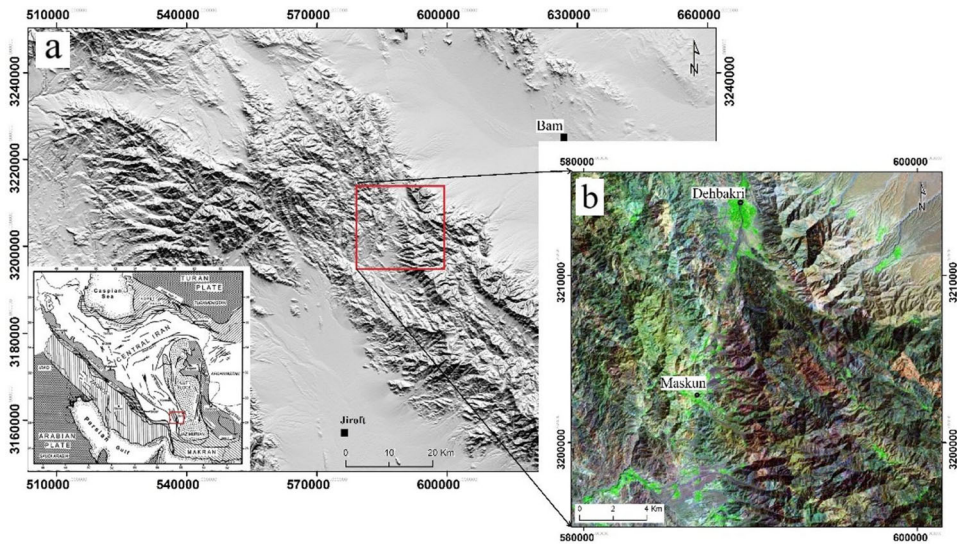
Figure 1. The study area's location in Iran as shown on (a) the shaded relief map and (b) the location of the Maskun village as shown on the satellite image.

area is located in the Lut watershed in the southwest of Iran and the Jebal Barez heights (Figure 1). The climate in Bam is hot and dry with some variations. Sometimes, it is the hottest place in Iran during the summer and the coldest place during the winter due to its proximity to the desert. Geologically, the Maskun landslide is located at Jebal Barez heights, mainly composed of Eocene volcanic rocks (Figure 2). Accordingly, the alternate layers of tuff, sandstone, and rhyolite are the major formations of the study area. Based on the tectonic division of Iran, the study area is located on the southern margin of the Lut block (Rashidi et al. 2019; Rashidi et al. 2021). This area is located along the path of the Gowk (Golbaf) strike-slip fault system (Rashidi et al. 2020), which forms the boundary between the Lut and central Iran blocks (Figure 2). Moreover, human activities in Maskun have increased the occurrence of landslides for about two decades, and many farmlands have been destroyed.

This study used Sentinel 1 A images for the PSI data processing incorporation with several field observations. The images (22 images) were acquired by the European Space Agency from November 5th, 2014, to June 24th, 2019 (Table 1). Besides, we used ENVISAT data to produce interferograms and maximum displacement (Table 2). We also collected rainfall and temperature data from the Iranian Meteorological Organization (IMO) to incorporate them with satellite images and then determine the relationships between mass displacement and climatic conditions. The monthly temperature and rainfall of Bam synoptic stations were from January 2000 to December 2019. The monthly average total rainfall varies from 14.6 mm to 92.7 mm per year. The monthly average means temperature varies from 23/61° C to 25.35° C.

3. Method

We used DInSAR and PSI techniques in this research. The techniques, strategy, and flowchart of this study are explained as follows.
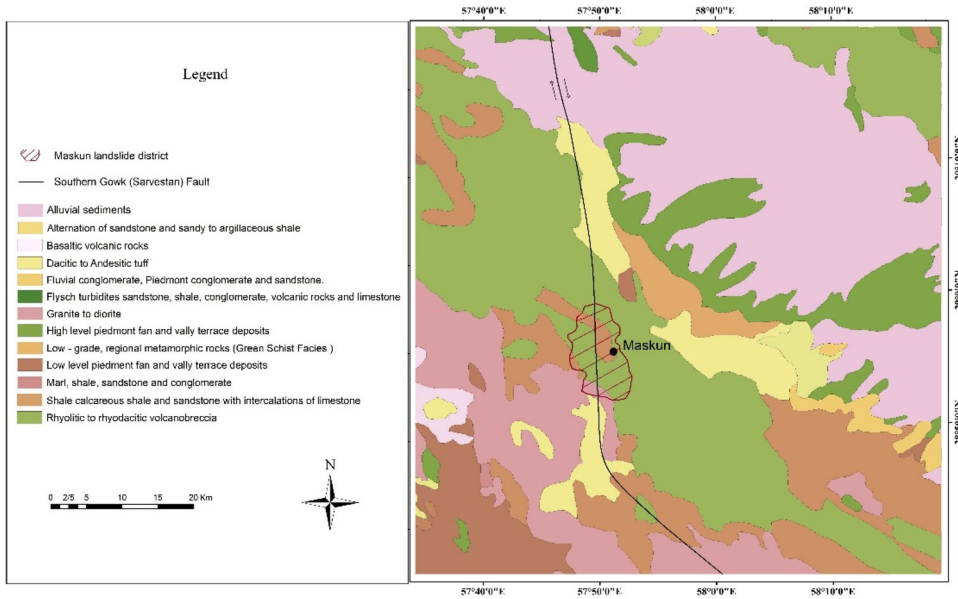
Figure 2. Geological map of the study area (Source: Iranian Surveying Organization) and Maskun landslide location relative to the Gowk Fault.

Table 1. Sentinel 1 A images used in the PSI.

No	Granule Name	Path Number	perpendicular (m)
1	S1A_IW_SLC__1SDV_20190624T020613_20190624T020640_027815_0323D2_25B0	93	−67
2	S1A_IW_SLC__1SDV_20190413T020610_20190413T020637_026765_0301AA_DABE	93	−52
3	S1A_IW_SLC__1SDV_20190131T020610_20190131T020637_025715_02DB98_326D	93	36
4	S1A_IW_SLC__1SDV_20181120T020612_20181120T020639_024665_02B5F5_FB06	93	−1
5	S1A_IW_SLC__1SDV_20180921T020612_20180921T020639_023790_02985C_D020	93	−4
6	S1A_IW_SLC__1SDV_20180804T020610_20180804T020637_023090_0281DF_7EE8	93	−61
7	S1A_IW_SLC__1SDV_20180605T020606_20180605T020633_022215_026746_E983	93	−100
8	S1A_IW_SLC__1SDV_20180406T020603_20180406T020630_021340_024BA0_70EB	93	−99
9	S1A_IW_SLC__1SDV_20180124T020603_20180124T020630_020290_022A54_51ED	93	−25
10	S1A_IW_SLC__1SDV_20171125T020605_20171125T020632_019415_020EE5_8118	93	15
11	S1A_IW_SLC__1SDV_20170914T020605_20170914T020632_018365_01EE91_A445	93	−1
12	S1A_IW_SLC__1SDV_20170728T020603_20170728T020630_017665_01D930_8886	93	0
13	S1A_IW_SLC__1SDV_20170610T020600_20170610T020627_016965_01C3E1_EFBB	93	52
14	S1A_IW_SLC__1SDV_20170505T020558_20170505T020625_016440_01B3B7_7F89	93	27
15	S1A_IW_SLC__1SDV_20170306T020556_20170306T020623_015565_01995E_91B1	93	−111
16	S1A_IW_SLC__1SSV_20161106T020600_20161106T020627_013815_01633F_E9D8	93	39
17	S1A_IW_SLC__1SSV_20160709T020602_20160709T020629_012065_012A8E_A552	93	−8
18	S1A_IW_SLC__1SSV_20160311T020548_20160311T020615_010315_00F44C_E8B9	93	−14
19	S1A_IW_SLC__1SSV_20151206T020550_20151206T020617_008915_00CC26_13E9	93	44
20	S1A_IW_SLC__1SSV_20150715T020541_20150715T020608_006815_0092D0_3305	93	−43
21	S1A_IW_SLC__1SSV_20150317T020536_20150317T020603_005065_0065C8_BDD6	93	35
22	S1A_IW_SLC__1SSV_20141105T020539_20141105T020606_003140_0039C1_76BC	93	−11

3.1. DInSAR technique

DInSAR is a microwave remote sensing technique that allows measuring surface deformation with centimeter to millimeter accuracy at high resolution (tens of meters) and large spatial coverage (Gabriel et al. 1989; Nobile et al. 2018). The DInSAR technique exploits the phase difference (interferogram) between two

Table 2. Summary of ENVISAT data used to produce interferograms and maximum displacement.

NO	Date	Frame	Track	Perpendicular Baseline (m)	Maximum displacement (mm/mth)
1	07092007 − 28082008	3033	392	14	5.3
2	27102007 − 12012008	3015	392	57	4.2
3	07012008 − 25042008	3033	392	31	6.8
4	17082008 − 21012009	3015	392	112	7.3
5	28012009 − 07052009	3033	392	37	7.2
6	24052009 − 11092009	3015	392	8	3.1
7	21102009 − 18102010	3015	392	87	5.4
8	10122009 − 05042010	3033	392	74	6.6
9	18042010 − 07072010	3033	392	128	3.7
10	09102010 − 15022011	3033	392	13	7.1
11	11022011 − 27092011	3033	392	135	4.1
12	01102011 − 14032012	3015	392	95	6.7
13	01112007 − 21032012	3015	392	23	5.2

temporally separated SAR acquisitions to measure the ground deformation along the radar LOS. Initially applied to characterize sizeable deformation events (Akbarimehr et al. 2013; Mehrabi et al. 2022), the DInSAR methodology has successively been adapted to analyze the temporal evolution of surface deformation via LOS displacement time series generation. Therefore, the information available from each interferometric SAR data pair must be properly related to that contained in other pairs by generating and inverting an appropriate sequence of DInSAR interferograms.

In general, there are three types of differential SAR interferometry. (i) Two-pass differential interferometry SAR, (ii) three-pass differential interferometry SAR, and (iii) four-pass differential interferometry SAR. Two-pass DInSAR uses an interferometric image pair and an external Digital Elevation Model (DEM). Among the two Single Look Complex (SLC) images, one is typically acquired before the surface displacement and the other after the event. The external DEM is converted to a corresponding phase image. This is illustrated in Figure 3, where P is the ground point in the two images. The sensor acquires the first SAR image (which is referred to as the master image) at time t_1, measuring the phase Φ_M, and then acquires a second SAR image (slave image) at time t_2, measuring the phase Φ_s. If the surface displacement occurred during this period, the point P is assumed to have moved to P_1.

After exploiting the phase difference between ΦM and Φs, one obtains the interferometric phase $\Delta\Phi$. As P moved to P_1 between the two images acquisitions, the $\Delta\Phi$ includes

$$\Delta\Phi = \Phi_{Topo} + \Phi_{Mov} + \Phi_{Atmos} + \Phi_{Noise} \qquad (1)$$

where Φ_{Topo} is the topographic phase component; Φ_{Mov} is the terrain change contribution; Φ_{Atmos} is the atmospheric delay contribution, and Φ_{Noise} is the phase noise. Two-pass DInSAR uses an external DEM to simulate the topographic phase Φ_{Topo_Simu}, and then the so-called DInSAR phase $\Delta\Phi_{DInSAR}$ can be computed:

$$\Delta\Phi D_{InSAR} = \Delta\Phi - \Phi_{Topo_{Simu}} = \Phi_{Mov} + \Phi_{Atmos} + \Phi_{Noise} + \Phi_{Res_{Topo}} \qquad (2)$$

where Φ_{Res_Topo} represents the residual component due to errors in the simulation of Φ_{Topo}. To derive information on the terrain change, Φ_{Mov} has to be separated from the other phase components. Three-pass interferometry can be used without prior known DEM but requires at least three images acquired of the same scene.
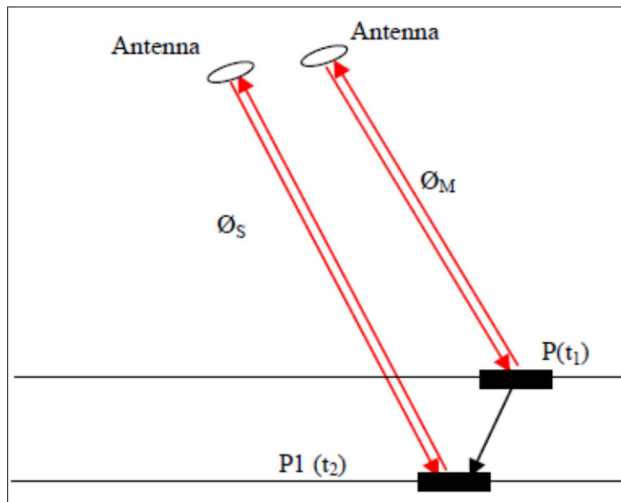
Figure 3. Principle of two-pass DInSAR. Where P is a ground point in the two images at time t_1 and t_2, the phases Φ_M and Φ_s are the master image phase and the slave image phase, respectively.

The technique used in this study is the differential interferometry SAR method (Zhang et al. 2020). In two passes, DInSAR just used 2 SAR images to calculate deformation, and then the DEM is processed to remove the topographic component and form an interferogram (Figure 4). To perform the two-pass DInSAR method step by step, the first two images are carefully mapped geometrically. Both images are georeferenced with each other. Then, the synthetic phase is created. The first image is a geometric reference, and the second image is a sub-image. Thus, a smoothed interferogram obtained contains an atmosphere that reduces the visual quality of the fringes. Each fringe shows a full-color cycle from blue (0 radians) to red (2π radians) via cyan, green, and yellow. It represents a single phase-difference cycle of 2π radians. Each fringe quantity is equal to half of the radar image wavelength. In the following, we use the adaptive filter to remove the atmospheric noise of smoothed interferogram for this purpose. This technique significantly improves the quality of the interferogram fringes. Also, it will remove the noises whose origin is due to the lack of correlation related to the baseline parameters. Also, the coherency map was prepared by filtering (a map or an image whose pixels show the correlation degree between two input signals for two images). The differential phase has measurement ambiguity to determine the earth's surface displacement, called torsion.

Since phase changes are measured as multiples of 2π (6.28) and the exact number of phase cycles will be lost in every measurement cycle; therefore, the interferogram will not become a deformation map without performing any process for recycling the lost cycles. Thus, this phase must be recovered for measures of more than 2π amounts. The recycling process disambiguates the phase (the recycled phase). This amount is proportional to the value of the deformation of the earth's surface perpendicular. For true conversion of the recycled phase to altitudinal values and the earth's surface calculation, it is necessary to perform the monitor phase, or second smoothing. Implementation of this phase causes possible circuit errors to be corrected and the amount of phase deviation to be calculated to determine the amount of absolute phase. GCP should be used
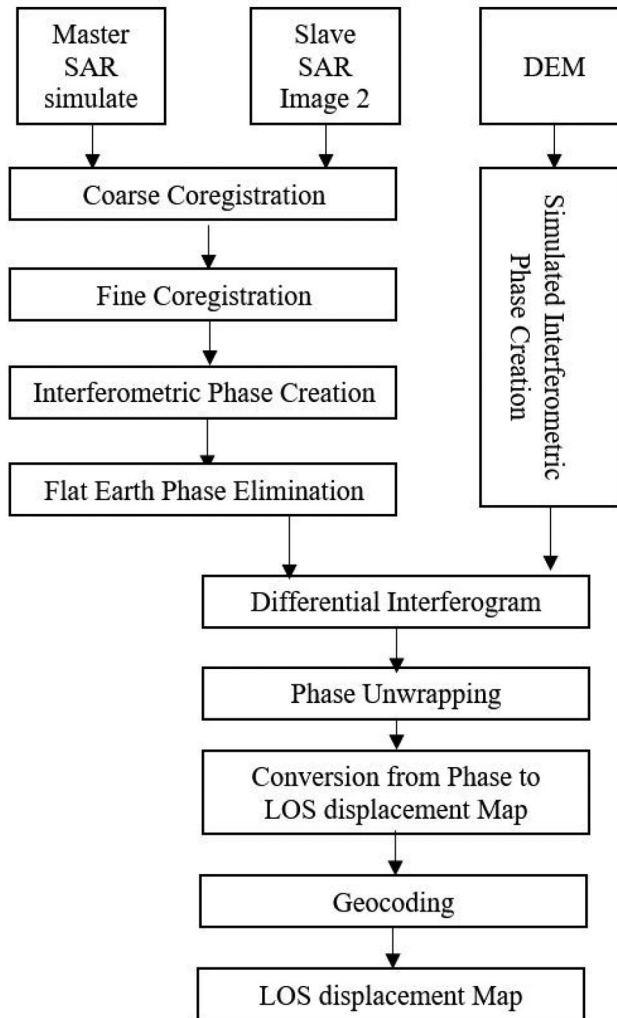
Figure 4. Block diagram of the DInSAR processing technique used for ASAR images.

for implementing this process. These points will be used to improve the necessary parameters in the settings of the monitoring processes, such as orbit error correction in sensors. Different steps of ASAR image analysis using the DInSAR technique to monitor and calculate the value of landslides have been shown in Figure 4.

3.2. PSI technique

The PS-InSAR method, as implemented in the SARscape software package, was used to perform interferometric processing of the SAR images in this study. The PS method works on the principle of identifying point targets represented as individual image pixels, known as Permanent Scatterers, that maintain high radar signal reflectivity over time. This method employs a stack of multi-temporal SAR acquisitions to improve the accuracy of displacement measurements and reduce errors caused by unstable atmospheric effects. For each point, a displacement time series and a mean
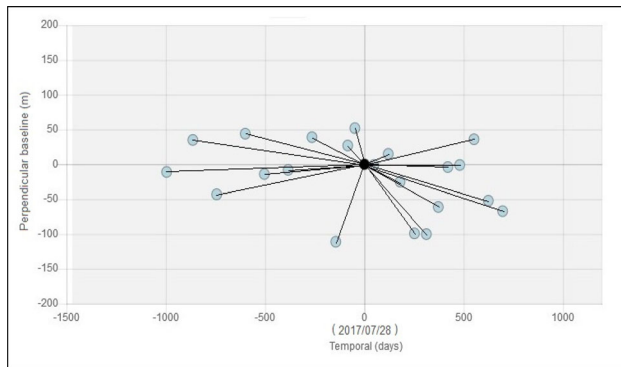
Figure 5. Examples of connection graphs between the master (black dot) and slave (Blue dots) images generated with the PS-InSAR approach. The graph is obtained from the descending Sentinel-1A/B dataset, track 93.

rapidity measure are calculated. In detail, the PS interferometric processing chain accepted in this research consists of the following stages:

The first step is to import images. In this stage, the Single Look Complex (SLC) images with radar amplitude and phase information in vertical co-polarization (VV) are imported. Precision circle files (Precise circle State Vectors for ENVISAT and Precise circle Ephemerides for Sentinel-1, both provided by the ESA, European Space Agency) are used to make corrections to the satellite's position. In the second stage, we attempted to generate a connection graph. To obtain the pairs and analyze them in the next stage, all of the images are linked to a master image (selected to minimize the spatial and temporal baselines across the dataset) (Figure 5).

The third stage is interferometric processing. In this stage, the images are co-registered to the geometry of the master image. The interferograms are then procreated by pixel-wise subtraction of the phase information in each image. The phase difference because of the topography is removed by using the Shuttle Radar Topographic Mission (SRTM) Digital Elevation Model (DEM) (1 arc second, $\sim$30 m $\times$ 30 m resolution). The remaining phase difference predominantly relates to atmospheric effects and ground displacement. The fourth stage is PSs identification. In this stage, the point goal candidates are identified by considering the Amplitude Dispersion Index (ADI), which is defined as the ratio between the standard deviation and the mean of the amplitude values of a pixel. Pixels with low ADI in all acquisitions are selected as PSs. The fifth stage is the First inversion. In this stage, the phase parts related to the topographic sedimentary and the displacement velocity are calculated using a linear velocity model and then removed from the interferograms. The relations (i.e., the measure of decorrelation because of temporal and geometric degradation and height of the image pixels) are also calculated. And the sixth step is the second inversion. The atmospheric phase parts are computed using the products of the linear model, which were calculated in the previous stage and then are subtracted from the interferograms by using high-pass (365 days) and low-pass (1200 m) filters. The PSs with relation values lower than 0.75 are discarded. Considering such parameters, the precision of the measured velocities was computed to be in the 0.06–0.39 mm/year range. The accuracy is computed from the following formula (3):
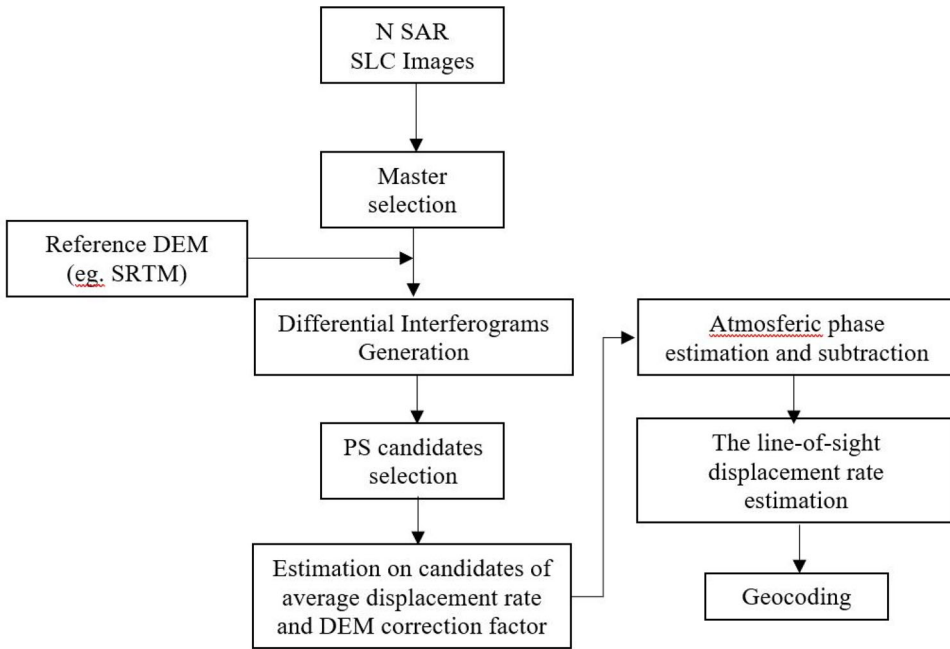
```
              ┌─────────────────┐
              │     N SAR       │
              │   SLC Images    │
              └─────────────────┘
                      │
                      ▼
              ┌─────────────────┐
              │     Master      │
              │   selection     │
              └─────────────────┘
┌─────────────────┐      │
│  Reference DEM  │      │
│  (eg. SRTM)     │──────┤
└─────────────────┘      │
                      ▼
              ┌─────────────────────┐       ┌──────────────────────┐
              │ Differential        │──────▶│  Atmosferic phase    │
              │ Interferograms      │       │ estimation and       │
              │ Generation          │       │ subtraction          │
              └─────────────────────┘       └──────────────────────┘
                      │                               │
                      ▼                               ▼
              ┌─────────────────┐           ┌──────────────────────┐
              │  PS candidates  │           │  The line-of-sight   │
              │   selection     │           │  displacement rate   │
              └─────────────────┘           │  estimation          │
                      │                     └──────────────────────┘
                      ▼                               │
              ┌──────────────────────┐                ▼
              │ Estimation on        │       ┌──────────────────────┐
              │ candidates of average │──────▶│     Geocoding        │
              │ displacement rate and │       └──────────────────────┘
              │ DEM correction factor │
              └──────────────────────┘
```

Figure 6. Block diagram of the exploited PS interferometric processing.

$$\sigma = \frac{\lambda}{4\pi} \sqrt{\frac{1-\gamma^2}{2\gamma^2}} \tag{3}$$

which σ is the calculated accuracy, λ is the signal wavelength, and γ is the average pixel coherence.

Velocities shown in the time-series plots below are reported to one significant digit, which thus represents a conservative estimate of the velocity accuracy. And finally, the seventh stage is geocoding. In this stage, the final interferometric products are geocoded into the WGS 1984 UTM zone 40 N projected coordinate system and exported as shape or raster files for the post-processing analyses (Fiaschi et al. 2019).

Considering the size and data volume, AOI-1 has been divided into sub-areas of around 10 km × 10 km, each processed independently. A ~10% overlap of these sub-areas was maintained to check the quality and consistency of the results. This method facilitated a more refined InSAR processing and produced more manageable results for the post-processing analyses.

Different processing steps to the PS interferometric for monitoring and calculating displacement tectonic are shown in Figure 6.

3.3. Relationship between landslide displacement and weather conditions

One of the factors affecting the behavior of slippery masses is soil moisture. Moreover, temperature and rainfall conditions are two influencing parameters that trigger landslides. Therefore, this study examined the relationships between the mentioned parameters quantitatively. For this purpose, the annual rainfall and
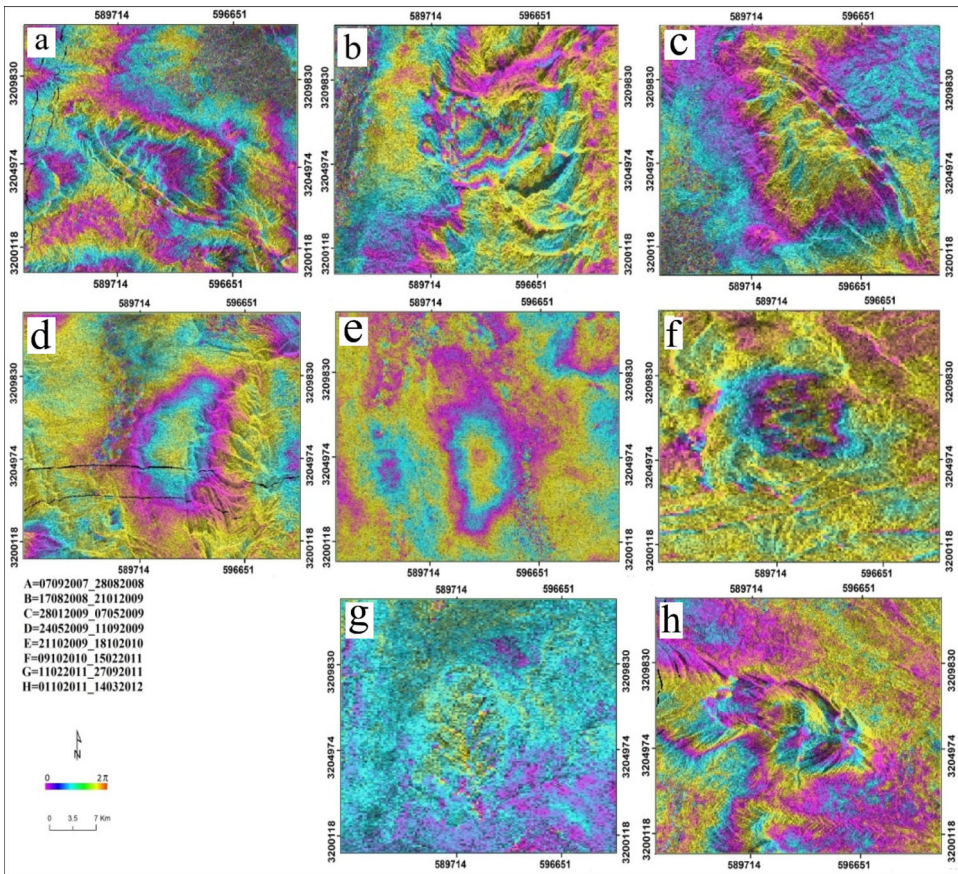
A=07092007_28082008
B=17082008_21012009
C=28012009_07052009
D=24052009_11092009
E=21102009_18102010
F=09102010_15022011
G=11022011_27092011
H=01102011_14032012

Figure 7. A view of the differential interferogram for highly coherent image pairs in different years using differential interferometry of ASAR images. (a) 07092007 – 28082008, (b) 17082008 – 21012009, (c) 28012009 - 07052009, (d) 24052009 - 11092009, (e) 21102009 - 18102010, (f) 09102010 - 15022011, (g): 11022011 - 27092011, (h) 01102011 – 14032012).

temperature statistics were collected and plotted. Besides, the diagram of landslide mass displacement behavior was prepared by using deformation time-series analysis. Similarly, we plotted the temperature and precipitation diagrams to investigate the correlation. Finally, the relationships between rainfall and landslide displacement rate were interpreted qualitatively and determined based on the time-series analysis and deformation pattern incorporated with the field observations.

4. Results

4.1. DInSAR techniques

We examined the capability and quality of the radar images used for making the interferogram by calculating the baseline values. Table 1 illustrates the results baseline values. Comparing the baseline critical and normal values showed that the images were suitable for use in interferometry processing. The image processing of topography effect removal from the interferogram and incorporating with ASTER DEM
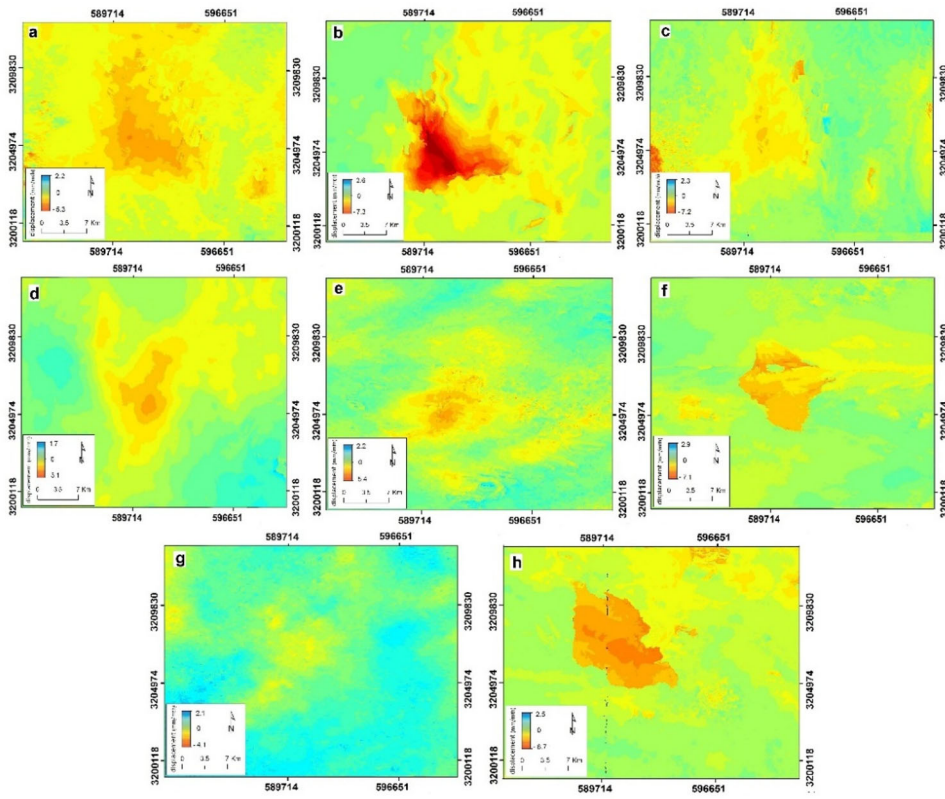
Figure 8. Landslide displacement rate maps at different time intervals. (a) 07092007 – 28082008, (b) 17082008 – 21012009, (c) 28012009 - 07052009, (d) 24052009 - 11092009, (e) 21102009 - 18102010, (f) 09102010 - 15022011, (g) 11022011 - 27092011, (h) 01102011 – 14032012).

30 m shows that a differential interferogram (DInSAR) is a flattened interferogram. Therefore, the fixed phase (due to the imaging geometry) and the topographic phase are removed from the interferogram. Since the flattened interferogram contains the noises that reduce the fringes' visual quality, the Goldstein adaptive filter was applied to remove the interferogram noise in the following. Then, we generated a coherence map by applying the Goldstein adaptive filter.

According to the results in Table 2, the selection of suitable image pairs (i.e., a pair of images whose vertical baseline is less than half of the critical highly coherent baseline). The DInSAR method was performed using the SARscape 5 software in ENVI 5 to provide a landslide displacement map for the relevant periods. Therefore, after performing the phase retrieval process, the phase was corrected by selecting the ground control points (GCPs) to remove the noise error. Then, to separate the deformation signal, the topography component was flattened and refined using the ASTER-DEM. For this purpose, the DEM was resampled with the main radar image and created a reference topography phase. The differential interferogram is obtained by subtracting the reference topography phase and the interferogram (flattened interferogram). This function is represented in the image by the fringes. Figure 7 shows a view of the differential interferogram derived from the subtraction of the reference
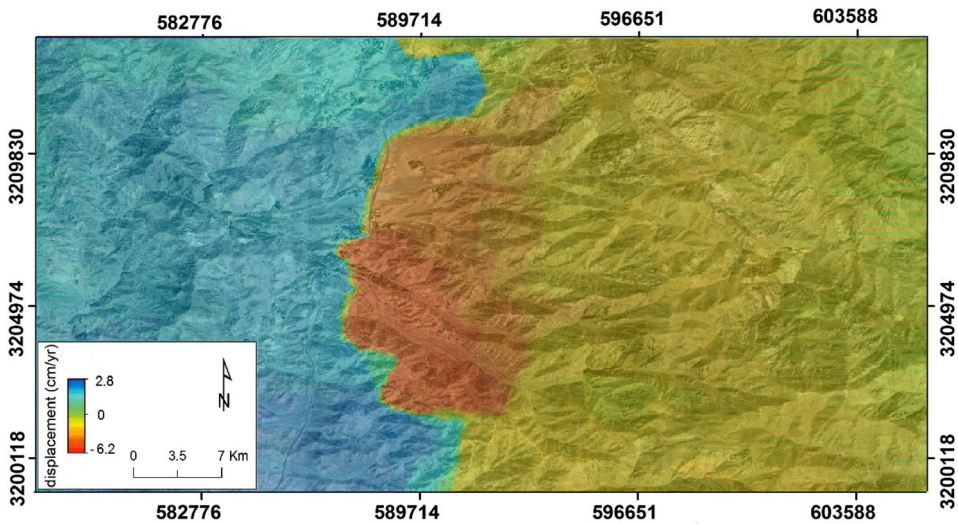
Figure 9. Average displacement level for Maskun landslide in period 2007-2012.

topography phase. The flattened interferogram is associated with high coherent image pairs and a larger landslide area in separate windows (Figure 7).

As illustrated in Figure 7, the fringes formed in the differential interferogram have a rather distinct pattern. The reason for this is the regular and continuous movement of the landslide mass over time. In general, it can be stated that the landslide that happened in this area occurs slowly, continuously, and gradually over time.

At the last step of the ASAR radar image processing, if suitable interferometry pairs can be created between different dates of the taken images, it would be possible to examine the level of landslides displacement when taking related images. Accordingly, the landslides displacement is presented using ASAR image processing (DInSAR) at different time intervals for some pairs of radar images during 2007-2012 in the form of phase-to-displacement conversion maps (Figure 8).

As illustrated in Figure 8, the displacement is defined as a range of numbers between the negative and positive millimeter values. For interpreting the results and estimating the displacement level, negative values represent depression or stripping levels within the range. Positive values indicate the accumulation of sediment at the foot of the slope. The results indicate that the maximum rate of displacement is 7.3 mm/month. Figure 8 (August 2008 and January 2009) shows the lowest displacement rate (3.1 mm/month) (Figure 8d) (May 2009 and September 2009). Accordingly, the average displacement level for the Maskun landslide over the entire study period is about 6.2 cm per year (Figure 9).

4.2. DInSAR Validation

The Validation of the proposed approach and DInSAR analysis results was done based on the GPS observations precise measurements in the Maskun vilage which belongs to National Cartographic Center (NCC) of Iran as the only GPS point station located in the study area. The GPS measurements of this point were carried out from 2007 to
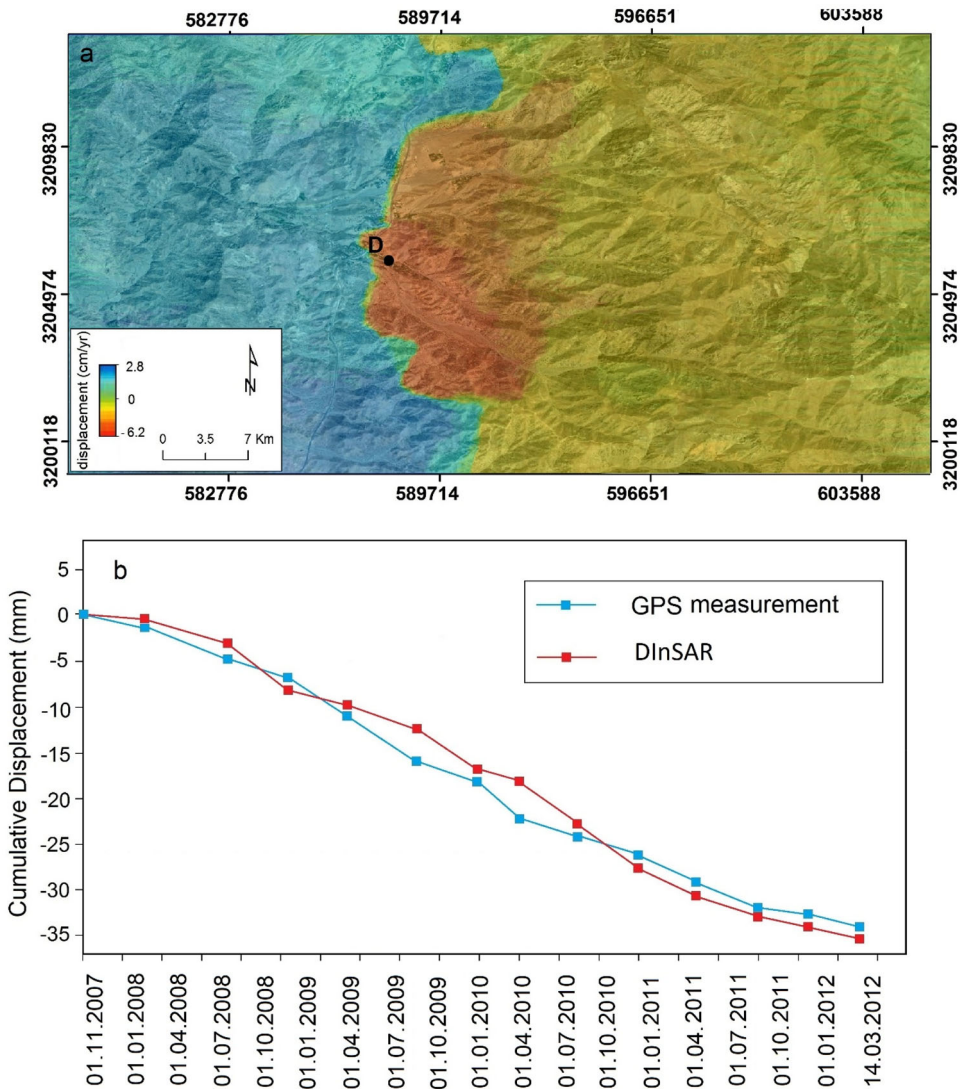
Figure 10. Comparison between DInSAR results vs. GPS measurements (b) on the point D shown in (a).

2012. We presented the time series of deformation for the GPS point station. However, the comparison of PSI results and GPS measurements reveals that the cumulative displacement measurement from DInSAR agrees with the cumulative displacement measurement from GPS (Figure 10). The misfit between the leveling GPS results data and time series analysis results was expressed as RMSE which estimated as 0.135 mm.

4.3. PSI techniques

For the PSI analysis, the multi-temporal series (Stack) of satellite images consists of 22 acquisitions spanning from 5 November 2014 to 24 June 2019. Pass direction of all images is Descending, Mode: IW, Product type: SLC.
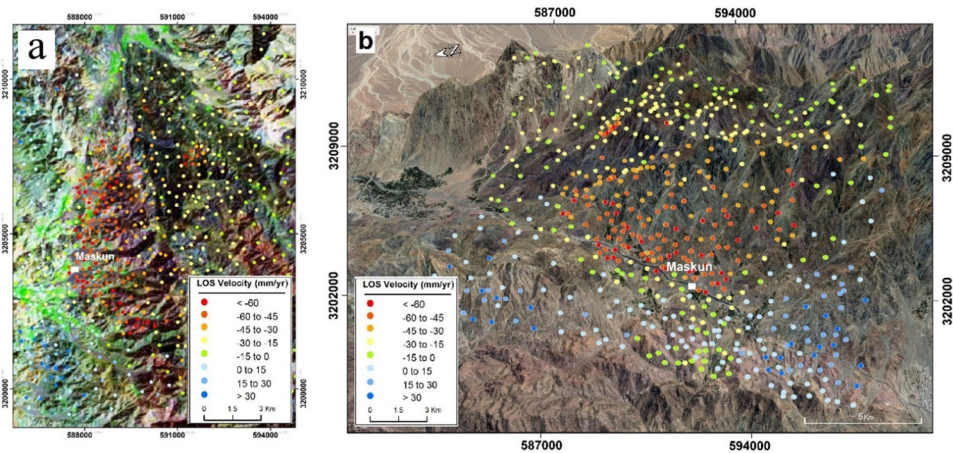
Figure 11. Deformation velocities at PS points in Maskun landslide identified by PS-InSAR from (a) Sentinel satellite data, and (b) PS points on the 3 D Google Earth view.

Ground displacement velocity map and time series are measured along the LOS of the satellite. The results refer to SAR acquisitions available only along a descending orbit. PSI has detected 770 points with coherence bigger than 0.75. The maximum LOS velocities detected by PSI are -64.5 mm year -1 (away from satellite) and 32.45 mm year -1 (toward to satellite) (Figure 11). Figure 11b is the Google Earth satellite image of the study area over which the dots are overlaid.

4.4. Climate condition

The results show that the average long-term precipitation in the study area is 60.86 mm/year over 20 years. According to the results, March is the highest rainfall month with an average of 11.84 mm, and August, with an average of 0.6 mm, is the driest month of the year. Figure 12 shows the distribution of monthly and annual precipitation in the study area.

Also, the results show that the long-term mean temperature of the Bam synoptic station is 23.35 °C. Also, July is the warmest month with an average temperature of 34.7 °C, and January with an average of 10.8 °C is the coolest month. Figure 12 shows the trend of annual and monthly temperature changes in the study area.

5. Discussion

The Maskun landslide is the only active landslide in the study area that has caused damage to roads and settlements. Therefore, in this study, D-InSAR and PSI techniques were used to identify the active limit of the landslide and calculate the displacement due to the landslide mass. Findings from the D-InSAR technique indicate that the Maskun landslide is moving at an average rate of 6.2 cm per year. The results also show the highest displacement occurred between August 2008 and January 2009, at a rate of 7.3 millimeters per month, and the lowest displacement took place between May 2009 and September 2009, at a rate of 3.1 millimeters per month. In general, the
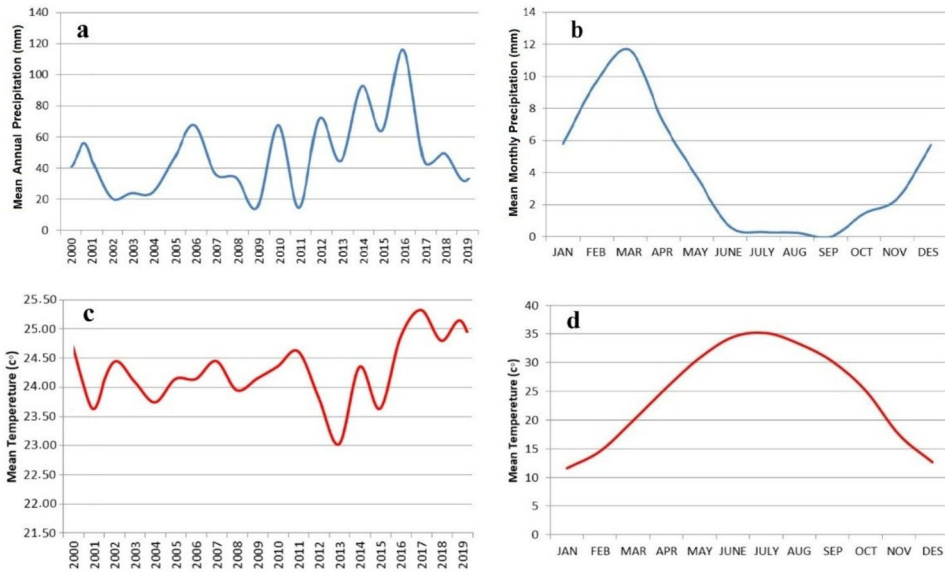
Figure 12. (a) Average annual precipitation of Bam synoptic station in the study area. (b) Average monthly precipitation of Bam synoptic station. (c) Average annual temperature graph of Bam synoptic station. (d) Average monthly temperature graph of Bam synoptic station.

results indicate that winter sliding mass displacement rates are greater than summer ones. For example, the displacement rate in the b, f, and h images (Figure 8) is higher, related to the region's winter and humid months. Also, the displacement rate is lower in the d and g images (Figure 8), related to the summer and low rainfall months in the region. Comparing these images with the average monthly and annual rainfall graphs (Figure 12) in the study area confirms the findings. In addition, the results of the deformation time series analysis of landslide mass and its comparison with rainfall diagrams prove this issue.

To analyze the spatio-temporal evolution of the Maskun landslide, we performed the cumulative deformation time series analysis from 5 November 2014 to 24 June 2019 (Figure 13). As illustrated in this figure, the area of the landslide mass continues to grow. Additionally, the displacement pattern is consistent with the local sandstone and shale rocks (see Figure 2). In addition, in terms of topography, the landslide district is concentrated in the Mountain foothills. As can be seen in Figure 13, the landslide is increasingly spreading into residential areas.

To investigate and monitor the movement of Maskun landslide mass over time, as well as to determine its relationship with rainfall, we conducted a deformation time-series analysis on a point in the center of the landslide. Figure 14 shows the analysis of data from 2007 to 2012 and from 2014 to 2019. Figure 14 illustrates the behavior of precipitation and landslide mass displacement. As illustrated in Figure 14, the displacement rate increased as rainfall increased and decreased as rainfall decreased. The slope of the displacement graph has increased in times when rainfall has increased and vice versa.

Moreover, the results of the analysis of Sentinel images using the PSI method show that in the study area, the maximum LOS velocities detected by PSI are −64.5 mm year − 1 (away from the satellite) and 32.45 mm year − 1 (toward the
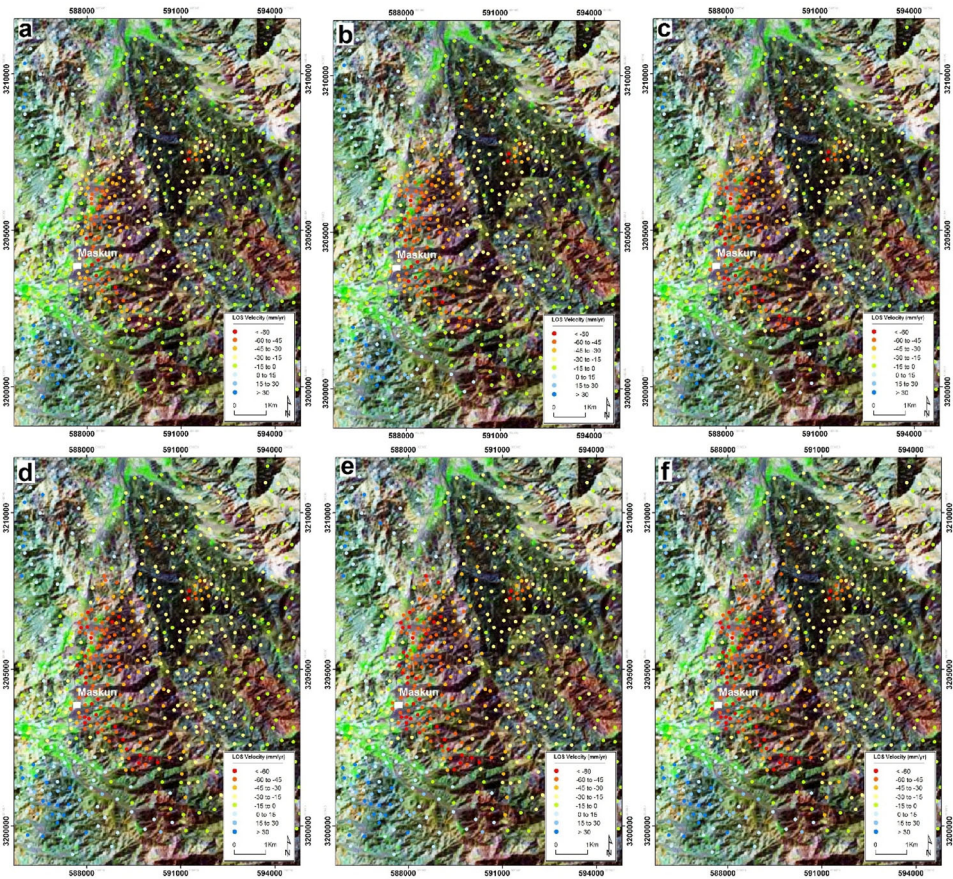
Figure 13. Cumulative deformation time series over the Maskun landslide from 5 November 2014 to 24 June 2019, (a): 20150715, (b): 20160709, (c): 20170306, (d): 20171125, (e): 20180921, (f): 20190624.
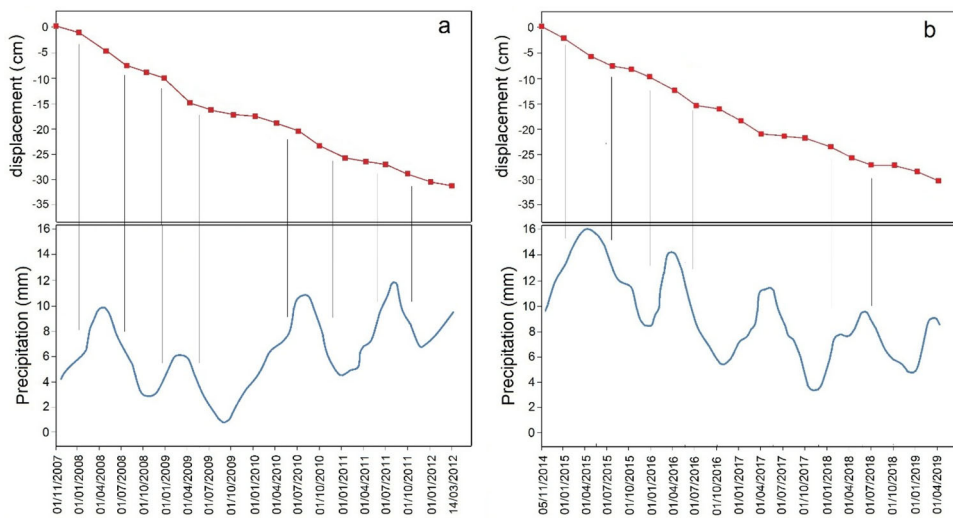

Figure 14. Deformation time-series analysis on a point in the center of the landslide for (a) 2007 to 2012 and (b) 2014 to 2019.

Figure 15. Activity area of Maskun landslide resulting from field surveys.

satellite). In general, the study findings revealed a continuous and active displacement of the Maskun landslide mass as seen on radar images, indicating that the slippery slope was gradually expanding from north to south. In addition, the landslide's spatial extent has grown over time, increasing from $130 \, \text{Km}^2$ in 2012 to $160 \, \text{Km}^2$ in 2019.

The results of the processing of SAR radar images, particularly in terms of defining a landslide area with the greatest displacement, were also consistent with field observations. Because of the climatic conditions and the location of the Maskun landslide area within the Gowk active fault (Figure 2), as well as active tectonics in the region, such as the continuous gas exhaust at a distance of $100 \, \text{m}$ from the landslide mass (Figure 15), tectonic activity may play a role in the occurrence of Maskun landslides. However, more research is needed to determine the role of tectonic activity in the Maskun landslide's occurrence.

6. Conclusion

A model and a framework were developed in this study that provide additional value to monitorimg landslides and determining the lack of investigation of the relationships between parameters. This is the first time that a correlation between parameters and quantitative relationships between the displacement rate of a landslide and weather conditions has been established in this area. Maskun landslide is an active landslide in the Dehbakri region of Bam, Iran, according to the findings of this study, and it requires additional attention in terms of natural disaster management and emergency preparedness. Using PSI and D-InSAR techniques, which are potential strategies for monitoring and detecting landslide mass deformation, this study concluded that combining techniques with climate parameters, such as rainfall and temperature, can determine the mass displacement behavior of the landslide. The weather has an impact on the Maskun landslide, according to the results of time series analysis. The majority of activity in the Maskun landslide occurs during the winter season, when the temperature is cooler and rainfall is greater than in other seasons. The role of tectonic activity and the Gowk Fault in triggering of landslides in the study area, on the other hand, should not be overlooked. As a result, this study recommends taking into account more climatic and geological factors, as well as combining In-SAR satellite images with new algorithms for automatic detection of mass movement direction and displacement.

ORCID

Mohsen Pourkhosravani 🔟 http://orcid.org/0000-0001-6181-6458
Ali Mehrabi 🔟 http://orcid.org/0000-0003-3287-7037
Saied Pirasteh 🔟 http://orcid.org/0000-0002-3177-037X
Reza Derakhshani 🔟 http://orcid.org/0000-0001-7499-4384

Data availability statement

The authors confirm that the data supporting the findings of this study are available within the article.

Disclosure statement

No potential conflict of interest was reported by the authors.

References

Akbarimehr M, Motagh M, Haghshenas-Haghighi M. 2013. Slope stability assessment of the Sarcheshmeh Landslide, Northeast Iran, Investigated using InSAR and GPS observations. Remote Sensing. 5(8):3681–3700.
Ali SA, Rangzan K, Pirasteh S. 2003. Use of digital elevation model for study of drainage morphometry and identification stability and saturation zones in relations to landslide assessments in parts of the Shahbazan area, SW Iran. Cartography. 32(2):71–76.

Azarafza M, Akgün H, Ghazifard A, Asghari-Kaljahi E, Rahnamarad J, Derakhshani R. 2021. Discontinuous rock slope stability analysis by limit equilibrium approaches–a review. Int J Digital Earth. 14(12):1918–1941.

Azarafza M, Azarafza M, Akgün H, Atkinson PM, Derakhshani R. 2021. Deep learning-based landslide susceptibility mapping. Sci Rep. 11(1):24112.

Azarafza M, Nanehkaran YA, Rajabion L, Akgün H, Rahnamarad J, Derakhshani R, Raoof A. 2020. Application of the modified Q-slope classification system for sedimentary rock slope stability assessment in Iran. Eng Geol. 264:105349.

Bianchini S, Herrera G, Mateos RM, Notti D, Garcia I, Mora O, Moretti S. 2013. Landslide activity maps generation by means of persistent scatterer interferometry. Remote Sensing. 5(12):6198–6222.

Bovenga F, Wasowski J, Nitti D, Nutricato R, Chiaradia M. 2012. Using COSMO/SkyMed X-band and ENVISAT C-band SAR interferometry for landslides analysis. Remote Sens Environ. 119:272–285.

Bru G, González PJ, Mateos RM, Roldán FJ, Herrera G, Béjar-Pizarro M, Fernández J. 2017. A-DInSAR monitoring of landslide and subsidence activity: A case of urban damage in Arcos de la Frontera, Spain. Remote Sens. 9(8):787.

Chaabani A, Deffontaines B. 2020. Application of the SBAS-DInSAR technique for deformation monitoring in Tunis City and Mornag plain. Geomatics Nat Hazards Risk. 11(1):1346–1377.

Chang K-J, Chan Y-C, Chen R-F, Hsieh Y-C. 2018. Geomorphological evolution of landslides near an active normal fault in northern Taiwan, as revealed by lidar and unmanned aircraft system data. Nat Hazards Earth Syst Sci. 18(3):709–727.

Crosetto M, Gili J, Monserrat O, Cuevas-González M, Corominas J, Serral D. 2013. Interferometric SAR monitoring of the Vallcebre landslide (Spain) using corner reflectors. Nat Hazards Earth Syst Sci. 13(4):923–933.

Farina P, Colombo D, Fumagalli A, Marks F, Moretti S. 2006. Permanent Scatterers for landslide investigations: outcomes from the ESA-SLAM project. Eng Geol. 88(3–4):200–217.

Fiaschi S, Holohan EP, Sheehy M, Floris M. 2019. PS-InSAR analysis of Sentinel-1 data for detecting ground motion in temperate oceanic climate zones: a case study in the Republic of Ireland. Remote Sens. 11(3):348.

Gabriel AK, Goldstein RM, Zebker HA. 1989. Mapping small elevation changes over large areas: Differential radar interferometry. J Geophys Res. 94(B7):9183–9191.

Hou L, Zhang Q. 2020. Velocity estimation of rock-fall in multi-channel SAR system with low PRF sampling. Geomatics Nat Hazards Risk. 11(1):535–543.

Liu P, Li Z, Hoey T, Kincal C, Zhang J, Zeng Q, Muller J-P. 2013. Using advanced InSAR time series techniques to monitor landslide movements in Badong of the Three Gorges region, China. Int J Appl Earth Observ Geoinform. 21:253–264.

Mehrabi A, Derakhshani R, Nilfouroushan F, Rahnamarad J, Azarafza M. 2022. Spatiotemporal subsidence over Pabdana coal mine Kerman Province, central Iran using time-series of Sentinel-1 remote sensing imagery. Episodes. accpted. https://doi.org/10.18814/epiiugs/2022/022009

Mehrabi A, Pirasteh S, Rashidi A, Pourkhosravani M, Derakhshani R, Liu G, Mao W, Xiang W. 2021. Incorporating persistent scatterer interferometry and radon anomaly to understand the anar fault mechanism and observing new evidence of intensified activity. Remote Sens. 13(11):2072.

Mehrabi A, Sadegh S, Pourkhosravani M, Derakhshani R. 2020. Tracking climatic changes using glacial traces and evidence at Hezar Mountain, Iran. SDMT. 12(2):246–256.

Mehrabi A. 2021. Monitoring the Iran Pol-e-Dokhtar flood extent and detecting its induced ground displacement using sentinel 1 imagery techniques. Nat Hazards. 105(3):2603–2617.

Nobile A, Dille A, Monsieurs E, Basimike J, Bibentyo TM, d'Oreye N, Kervyn F, Dewitte O. 2018. Multi-temporal DInSAR to characterise landslide ground deformations in a tropical urban environment: Focus on Bukavu (DR Congo). Remote Sens. 10(4):626.

Novellino A, Cesarano M, Cappelletti P, Di Martire D, Di Napoli M, Ramondini M, Sowter A, Calcaterra D. 2021. Slow-moving landslide risk assessment combining Machine Learning and InSAR techniques. Catena. 203:105317.

Rashidi A, Abbassi M-R, Nilfouroushan F, Shafiei S, Derakhshani R, Nemati M. 2020. Morphotectonic and earthquake data analysis of interactional faults in Sabzevaran Area, SE Iran. J Struct Geol. 139:104147.

Rashidi A, Khatib MM, Nilfouroushan F, Derakhshani R, Mousavi SM, Kianimehr H, Djamour Y. 2019. Strain rate and stress fields in the West and South Lut block, Iran: Insights from the inversion of focal mechanism and geodetic data. Tectonophysics. 766: 94–114.

Rashidi A, Kianimehr H, Shafieibafti S, Mehrabi A, Derakhshani R. 2021. Active faults in the west of the Lut block (Central Iran). Geophys Res. 22(3):70–84.

Schlögel R, Doubre C, Malet J-P, Masson F. 2015. Landslide deformation monitoring with ALOS/PALSAR imagery: A D-InSAR geomorphological interpretation method. Geomorphology. 231:314–330.

Wang G, Xie M, Chai X, Wang L, Dong C. 2013. D-InSAR-based landslide location and monitoring at Wudongde hydropower reservoir in China. Environ Earth Sci. 69(8):2763–2777.

Zhang Q, Wang J, Hou L, Lin P, Song S. 2020. A novel method of dynamic monitoring and parameter estimation for rock-fall based on multichannel SAR. Geomatics Nat Hazards Risk. 11(1):619–631.

Zhang Y, Meng X, Dijkstra T, Jordan C, Chen G, Zeng R, Novellino A. 2020. Forecasting the magnitude of potential landslides based on InSAR techniques. Remote Sens Environ. 241: 111738.

Zhu Q, Chen L, Hu H, Pirasteh S, Li H, Xie X. 2020. Unsupervised feature learning to improve transferability of landslide susceptibility representations. IEEE J Sel Top Appl Earth Observations Remote Sens. 13:3917–3930.